Three-Dimensional Analysis of Macrovoids Formed by Nonsolvent-Induced Phase Separation (NIPS) Using X-ray Microcomputed Tomography (Micro-CT)

Sadaki Samitsu, Misa Hazutani, Miwa Ohniwa*

Research Center for Macromolecules and Biomaterials, National Institute for Materials Science, 1-2-1 Sengen, Tsukuba, Ibaraki 305-0047, Japan

Corresponding author: SAMITSU.Sadaki@nims.go.jp

Keywords: nonsolvent-induced phase separation (NIPS); macrovoid; X-ray microcomputed tomography (micro-CT); three-dimensional structural characterization; membrane formation mechanism

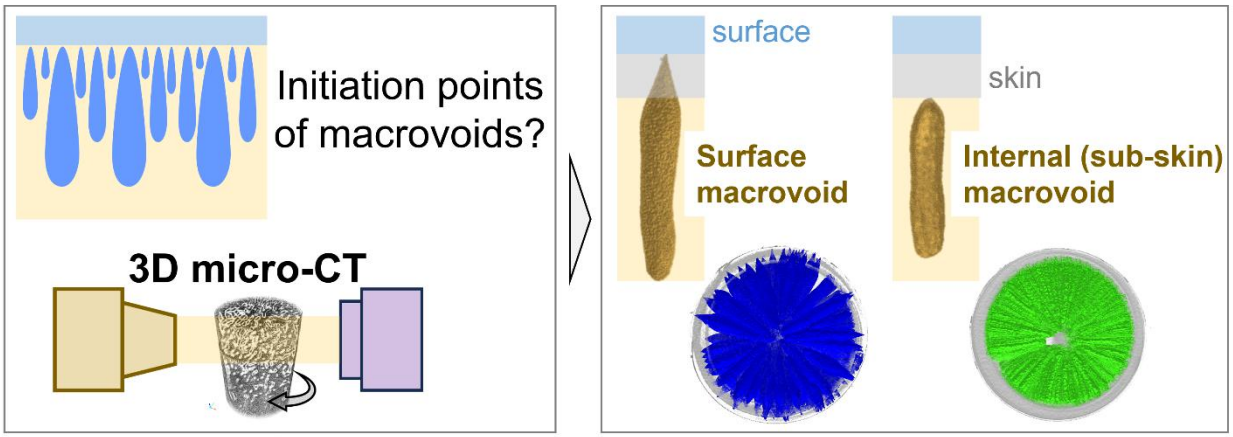

ABSTRACT Macrovoids formed by nonsolvent-induced phase separation (NIPS) critically influence the fabrication of polymer membranes and fibers. Numerous studies have been conducted on fabrication parameters, various formation mechanisms have been proposed, and recent simulation studies have advanced our understanding of formation kinetics. However, structural characterization of macrovoid formation remains limited due to semi-quantitative analysis based on two-dimensional observations using optical microscopy and scanning electron microscopy. Here, we employ high-resolution X-ray microcomputed tomography (micro-CT) to directly visualize and quantitatively analyze macrovoids in three dimensions over a sufficiently large field of view. Three-dimensional micro-CT observations reveal the existence of two distinct types of macrovoids with fundamentally different initiation locations and geometries: surface macrovoids that initiate at or near the membrane surface with sharp initiation tips, and internal (sub-skin) macrovoids that nucleate beneath the skin layer with rounded initiation geometries. Based on three-dimensional image data, depth profiles of macrovoid structural parameters were quantitatively analyzed. This study demonstrates X-ray micro-CT as a powerful

experimental approach for elucidating phase-separation phenomena and guiding the rational design of macroporous structures in polymer membranes and fibers.

1. INTRODUCTION

The nonsolvent-induced phase separation (NIPS) method is widely used to fabricate porous membranes [1–3] and fibers [4]. During NIPS, exchange between solvent and nonsolvent triggers phase separation into polymer-rich and polymer-lean domains, often producing elongated polymer-lean regions referred to as macrovoids. Macrovoids contain finger-like anisotropic channels that range from a few to several tens of micrometers in width, and from several tens to several hundred micrometers in length[5]. Because macrovoids can influence permeation pathways and mechanical integrity, describing their morphology and spatial distribution is important for controlling porous architectures and optimizing processing conditions.

Key process parameters have been reported to affect macrovoid formation in NIPS. Macrovoid formation can be suppressed by increasing the polymer concentration [6–9], adding a solvent to the coagulation bath [5,7,10], adding a nonsolvent to the polymer solution [10–12], using a solvent that is less miscible with the nonsolvent in the coagulation bath [7,10,13,14], lowering the temperatures of the casting solution and coagulation bath[2,6,15], introducing organic additives such as polyvinylpyrrolidone into the polymer solution [16,17], or increasing the solvent evaporation time prior to immersion [18,19]. These empirical trends provide practical guidance for morphology control, yet a quantitative description of macrovoid architectures remains challenging.

Over the past 50 years, a variety of mechanisms for macrovoid formation during NIPS have been proposed, and these mechanisms have been examined through extensive experimental and theoretical studies. Surface-initiated scenarios emphasize interfacial instabilities [19,20], convective flow [6], and hydrodynamic fingering near the membrane–coagulation-bath interface [21–23], which can trigger finger-like void growth propagating normal to the surface in the early stages of phase

separation. In contrast, internally initiated scenarios attribute macrovoid formation to phase separation beneath the thick skin layer, where polymer-lean nuclei initiate and subsequently grow in the interior [10,16,24]. Several studies have also suggested that macrovoids may arise from multiple mechanisms rather than a single universal process [8,25]. Complementary simulation studies incorporating diffusion, phase separation, and hydrodynamic transport further indicate that changes in fabrication conditions can shift the dominant phase-separation pathway, leading to different macrovoid structures [23,26–32].

Although simulations have provided valuable mechanistic insights, structural characterization of macrovoids has remained semi-quantitative because it relies heavily on two-dimensional observations such as scanning electron microscopy (SEM) [7,19] and optical microscopy,[5,19,25] which makes it difficult to identify initiation locations and to reconstruct the three-dimensional geometries and spatial distributions of individual macrovoids [33,34]. Recently, three-dimensional imaging techniques have emerged as powerful tools for resolving complex morphologies in phase-separated polymer structures,[34–38] yet the application of these techniques to quantitative macrovoid analysis remains limited. Brickey *et al.* employed FIB–SEM tomography to obtain stacked slices from the macrovoid-free near-surface region to depths of several micrometers and analyzed depth-dependent nanopore porosity and connectivity[39]. Górecki *et al.* used ptychographic X-ray computed tomography (PXCT) to quantify the depth-dependent porosity from the surface to 80 μm depth with a spatial resolution of 26 nm[36]. To elucidate macrovoid architectures at the population level, it is necessary to capture a sufficient number of macrovoids within the field of view in order to quantify their individual morphologies as well as their spatial distributions and mutual relationships.

Herein, we employ high-contrast, high-resolution X-ray microcomputed tomography (micro-CT) to directly visualize and quantitatively analyze macrovoid structures in three dimensions. Polyacrylonitrile (PAN) fibers were fabricated by NIPS and used as axisymmetric specimens suitable for micro-CT imaging. We show that two types of macrovoids can be consistently distinguished depending on fabrication conditions: surface macrovoids that initiate at or near the surface with sharp tips, and internal (sub-skin) macrovoids that nucleate beneath the skin layer with rounded initiation geometries. Depth-resolved quantitative analysis reveals that the number density, size distribution, and spatial arrangement of these macrovoid populations vary systematically with polymer concentration and dope-solution composition. Overall, micro-CT offers a practical, quantitative, depth-resolved framework for comparing macrovoid architectures across processing conditions.

2. EXPERIMENTAL SECTION

Only the key experimental procedures are described here; full details are provided in the Supporting Information.

2.1. Materials

PAN (M_w = 150,000) was purchased from Scientific Polymer Products, Inc.

2.2. Fiber Spinning

PAN solutions in DMSO were wet-spun into a water coagulation bath at room temperature using a syringe dispenser (ML-5000XII, Musashi Engineering, Japan) (Scheme 1). Process parameters are summarized in Table S1. The as-spun fibers were post-treated in water at 60 °C for 1 h, collected, and air-dried for 1 d. Without post-treatment, fiber diameters decreased by 20–25% upon drying, whereas hot-water post-treatment yielded dry fibers with diameters within

97% of the wet values. Dry fibers with diameters of 0.40–0.60 mm were prepared so that the entire cross-section fit within the field of view on micro-CT imaging.

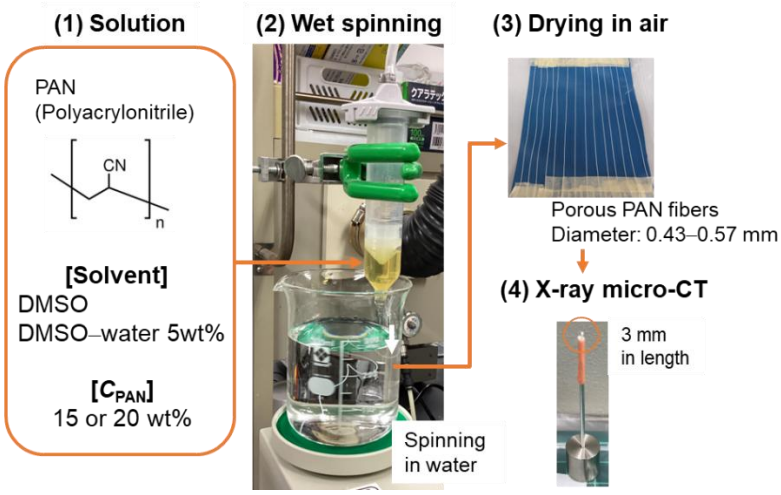

Scheme 1. Schematic depicting the experimental procedure used in this study.

2.3. Characterization

The total porosity of a dry fiber (ϕ_{bulk}) was calculated from the measured bulk density (ρ_{bulk}) and the true density of PAN (ρ_0 = 1.18 g/cm³) [40] using ϕ_{bulk} (%) = [1 − ρ_{bulk} / ρ_0] × 100. Fiber cross-sections were prepared by freeze fracture, platinum-coated, and observed by SEM (S-4800, Hitachi, Japan). Freeze fracturing minimizes deformation during sectioning and enables SEM imaging of the native nanoporous morphology; however, the fracture plane can vary between samples, making it difficult to reproduce macrovoid morphologies quantitatively from SEM images alone.

Table 1. Fabrication conditions and structural characteristics of wet-spun PAN fibers

Sample ID	PAN-15	PAN-20	PAN-15w

C_p (wt%)	15	20	15
Solvent	DMSO	DMSO	DMSO-water 95:5 (wt%)
ϕ_{bulk} (%)	75.6	68.5	76.2
ϕ_{CT} (%)	44.6	23.2	32.1
ϕ_{nano} (%)	31.0	45.3	44.1
$\phi_{skeleton}$ (%)	56.0	59.0	64.9
L_{skin} (μm)	3.6	46.9	37.7

C_p: PAN concentration in the dope solution; ϕ_{bulk} and ϕ_{CT}: porosities determined by bulk density measurements and from CT data, respectively; ϕ_{nano}, nanoporosity of the polymer skeleton, defined as $\phi_{nano} = \phi_{bulk} - \phi_{CT}$; $\phi_{skeleton}$: porosity of the polymer skeleton $\phi_{skeleton} = 100 \times \phi_{nano} / (100 - \phi_{CT})$; L_{skin}: CT-determined thickness of the skin layer orthogonal to the fiber axis.

2.4. X-ray Micro-CT Imaging and Image Analysis

Micro-CT data were acquired using a high-resolution X-ray microscope (nano3DX, Rigaku, Japan) with an X-ray wavelength of 1.5 Å.[41] The voxel size of the 3D image was 0.64 μm. Three-dimensional datasets were analyzed using ExFact VR (Nihon Visual Science, Japan) with the void-analysis option. Macrovoids were segmented by watershed using multiple intensity thresholds (Scheme 2a,b), following our previous work.[42] Macrovoid size was quantified using the volume of each segmented macrovoid, $v_{void} = n_{void}\ v_{voxel}$, and expressed as an equivalent spherical diameter (d_{3D}) calculated from v_{void} as $d_{3D} = (6\ v_{void} /\pi)^{1/3}$, where n_{void} is the number of voxels assigned to a given macrovoid and v_{voxel} is the volume of a single voxel. For visualization, macrovoids were color-coded by d_{3D} (and the corresponding v_{void} range): purple, <10 μm (v_{void} < 524 μm³); blue, 10–20 μm (524–4,189 μm³); green, 20–50 μm (4,189–65,450 μm³); yellow, 50–

100 μm (65,450–523,599 μm³); and red, >100 μm (v_{void} > 523,599 μm³). The porosity determined from micro-CT (ϕ_{CT}) was calculated as ϕ_{CT} (%) = N_{void} / N_{total} × 100, where N_{void} is the total number of voxels assigned to macrovoids and N_{total} is the total number of voxels in the specimen volume, including both macrovoid and polymer-skeleton regions. Because the present micro-CT analysis resolves pores larger than a few micrometers, ϕ_{CT} represents the macrovoid contribution, whereas ϕ_{bulk} includes pores across all length scales. The nanoporosity of the polymer skeleton was estimated as $\phi_{nano} = \phi_{bulk} - \phi_{CT}$, and the porosity of the polymer skeleton was defined as $\phi_{skeleton} = 100 \times \phi_{nano} / (100 - \phi_{CT})$. The skin layer thickness (L_{skin}) is defined as the distance from the surface to the macrovoid region in the CT image (Scheme 2b).

2.5. Development Views and Depth-Resolved Analysis

2D cross-sectional views (development views) of concentric circles were generated from the 3D datasets at 5 μm intervals from the fiber surface along the depth direction (Scheme 2c) and exported as sequential images. Macrovoids and polymer skeleton regions were analyzed in MIPAR software (MIPAR Image Analysis, USA) using threshold values determined by ExFact VR void analysis; the resulting binary images were cross-checked against the corresponding grayscale images. From each development view, the circular equivalent macrovoid diameter (d_{2D}), local thickness of the polymer skeleton (w_{av}, obtained using a local-thickness algorithm), average inter-macrovoid spacing (b_{av}), macrovoid number density (n_{void}), and macrovoid area fraction (f_{void}), were calculated using the measurement functions of MIPAR.[41]

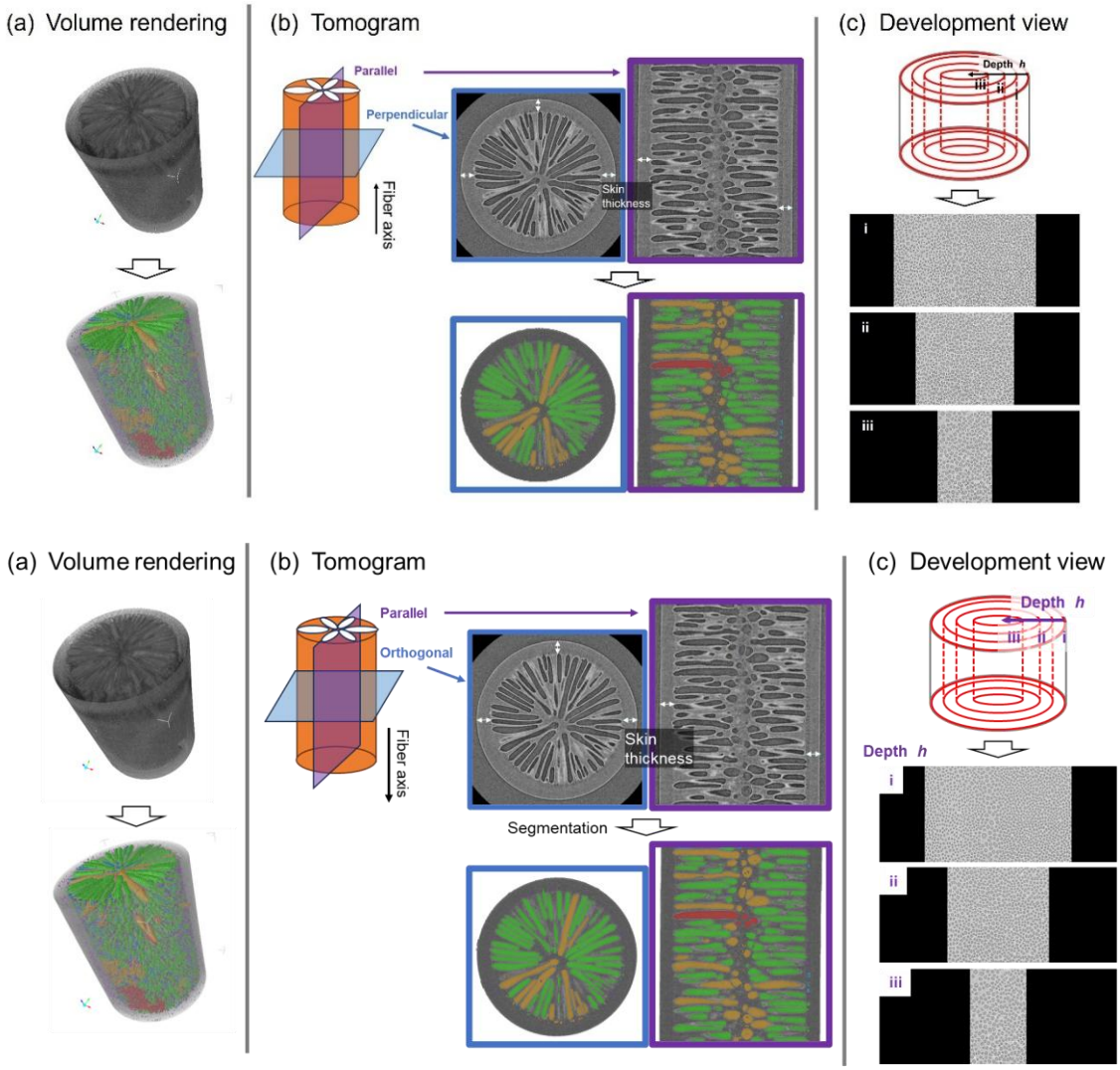

Scheme 2. Visualization modes of the X-ray micro-CT data used in this study. (a) Volume-rendering views displaying 3D data in two dimensions. The original micro-CT dataset consists of grayscale voxel intensities. After segmentation, each macrovoid is assigned a color label based on its three-dimensional equivalent diameter, d_{3D}: purple, <10 μm; blue, 10–20 μm; green, 20–50 μm; yellow, 50–100 μm; and red, >100 μm. (b) Representative tomograms taken parallel and orthogonal to the fiber axis. (c) Development views sequenced in the depth direction.

3. RESULTS AND DISCUSSION

3.1. 3D Visualization of Macrovoids

SEM images of a PAN15 fiber revealed numerous macrovoids extending from the fiber surface into the interior (Figure 1a, S2). Near the surface, macrovoids are thin and densely distributed, whereas deeper in the fiber, they become fewer in number but larger in size. The inter-macrovoid PAN skeleton exhibits a nanoporous structure (Figure 1b) similar to that of the flat-sheet porous PAN membrane formed by NIPS [43].

Micro-CT images clearly enabled the porous morphologies of the macrovoids to be visualized in a non-destructive manner owing to differences in X-ray attenuation contrast (Figure 1c,d); here, the light- and dark-gray regions correspond to the polymer skeleton and air, respectively. Because nanopores within the skeleton were comparable to or smaller than the voxel size, no discernible pore features were observed within the skeletal regions in the micro-CT images. Tomograms acquired parallel and perpendicular to the fiber axis clearly show the surface skin layer as bright gray regions. The thickness of the skin layer was measured at an average of 3.6 μm (Table 1), which is comparable to previously reported values [2,44].

The macrovoids were largely unconnected to each other; consequently, they were appropriately segmented as isolated voids using a watershed algorithm based on brightness differences (Figure 1e,f) [42]. A comparison of Figures 1c and 1e reveals that the dark-gray regions in the tomogram were appropriately segmented as macrovoids; this segmentation process enables the visualization of macrovoids by coloring them according to volume, while simultaneously allowing the skeletal structure itself to be displayed transparently through 3D volume rendering (Figure 1f). Macrovoid porosity, ϕ_{CT}, was determined to be 44.6% from the 3D CT data, which is much smaller than the ϕ_{bulk} value of PAN-15, namely 75.6% (Table 1). Based on the ϕ_{CT} and ϕ_{bulk} values, ϕ_{nano} and $\phi_{skeleton}$ were calculated to be 31.0% and 56.0%, respectively. Nanopores within the skeleton are visible in SEM images (Figure 1b); however, quantitative evaluation of

the nanoporosity based on SEM image analysis typically requires extensive image processing and thresholding, which can be time-consuming. Micro-CT provides a convenient approach to estimate nanoporosity by comparing the total porosity with the macrovoid porosity in three dimensions.

We confirmed that macrovoids with similar structures formed along the fiber axis, which involved visualizing them by overlaying several thin cross-sections along the fiber axis and moving them in the axial direction. Macrovoids classified according to volume were visualized individually, which facilitated recognition of the spatial arrangement and shape characteristics of each macrovoid (Figure S1). Macrovoids grew from the surface and extended linearly toward the central axis of the fiber, irrespective of size. Small macrovoids were only found to be distributed near the surface, whereas fewer larger voids that extended more deeply into the center of the fiber were observed. Many macrovoids initiated on the surface and grew in the depth direction, resulting in competitive growth between adjacent macrovoids that resulted in the formation of dense linearly elongated macrovoids in the depth direction (Figure 1g).

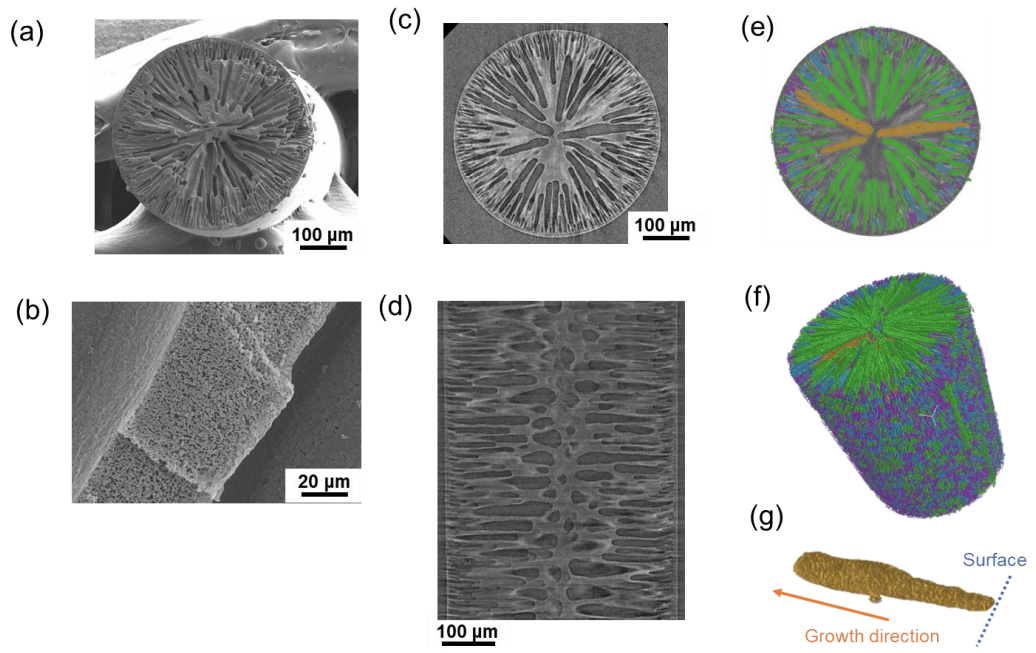

Figure 1. Cross-sectional SEM and micro-CT images of a PAN-15 fiber. (a) SEM micrograph showing the full fiber cross section. (b) Higher-magnification SEM image of the nanoporous PAN skeleton between adjacent macrovoids. Grayscale micro-CT tomograms acquired (c) perpendicular to and (d) parallel to the fiber axis. (e) Color-labeled segmentation map corresponding to panel (c), with macrovoids classified by size. (f) Volume-rendered macrovoid population in PAN-15. (g) Volume-rendered image of a representative macrovoid that initiated from the surface and grew in the depth direction.

3.2. Depth Profiles of Macrovoid Structural Parameters for Thin-Skinned Fibers

Development views from the 3D volume data enabled changes in macrovoid cross-section to be tracked in the depth direction, *h*, from the surface (Scheme 2c). Macrovoids and polymer skeletons are easily recognized as dark- and light-gray regions, respectively, in the development views (Figure 2a). Macrovoids appear as isolated dark closed circles that correspond to cross-sections orthogonal to their long axes; consequently, quantifying their number and diameter as

functions of h is easily achieved through 2D image analysis. Small and densely distributed macrovoids are observed near the surface (h = 50 μm), whereas fewer but larger macrovoids are found deeper in the fiber (h = 150 μm). Both images reveal macrovoids with uniform, almost circular cross-sections; their equivalent circular diameters, d_{2D}, which were calculated from the cross-sectional areas of the macrovoids, exhibit single narrow distributions with average d_{2D} values of 9.6 and 16.0 μm at h = 50 and 150 μm, respectively (Figure 2b). The observed increase in cross-sectional diameter with increasing h is consistent with the 3D image (Figure 1g) that shows that macrovoids grow into elongated conical shapes.

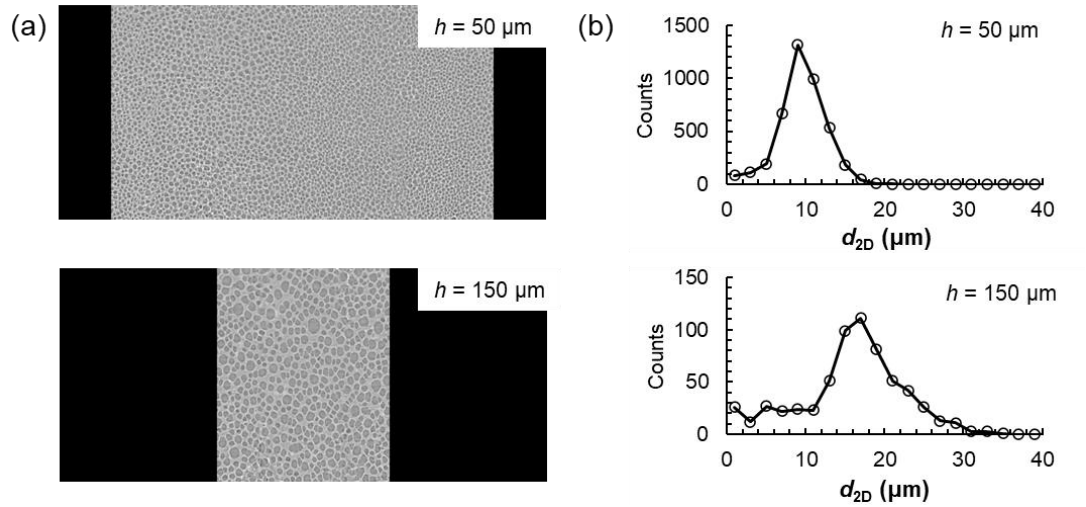

Figure 2. (a) Development views of PAN-15 at different depths, h, from the surface. Grayscale brightness was manually adjusted for naked-eye-viewing clarity. (b) Equivalent circular diameter, d_{2D}, distributions calculated from macrovoid cross-sectional areas (upper, h = 50 μm; lower, h = 150 μm).

Depth profiles of structural characteristics were calculated according to the sequential development views (Figure 3). The average value of d_{2D} was calculated to be 7.7 μm at h = 25 μm; this value increased linearly to 16.0 μm at h = 150 μm. The resulting plot was linearly fitted to afford: $d_{2D} = 0.064\ h + 6.59$. w_{av} and b_{av} increased linearly with h according to: $w_{av} = 0.047\ h$

+ 1.34 and b_{av} = 0.116 h + 8.0. The slopes of the d_{2D} and w_{av} plots add up to the slope of the b_{av} plot, consistent with the single-peak distributions exhibited by d_{2D} and w_{av}. n_{void} decreases monotonically with h and is inversely proportional to h (Figure 3d). Consequently, f_{void} was found to be independent of h and remained nearly constant at 57%. This value is higher than the ϕ_{CT} value (44.6%) because the ϕ_{CT} includes the central fiber region, where macrovoids are less abundant.

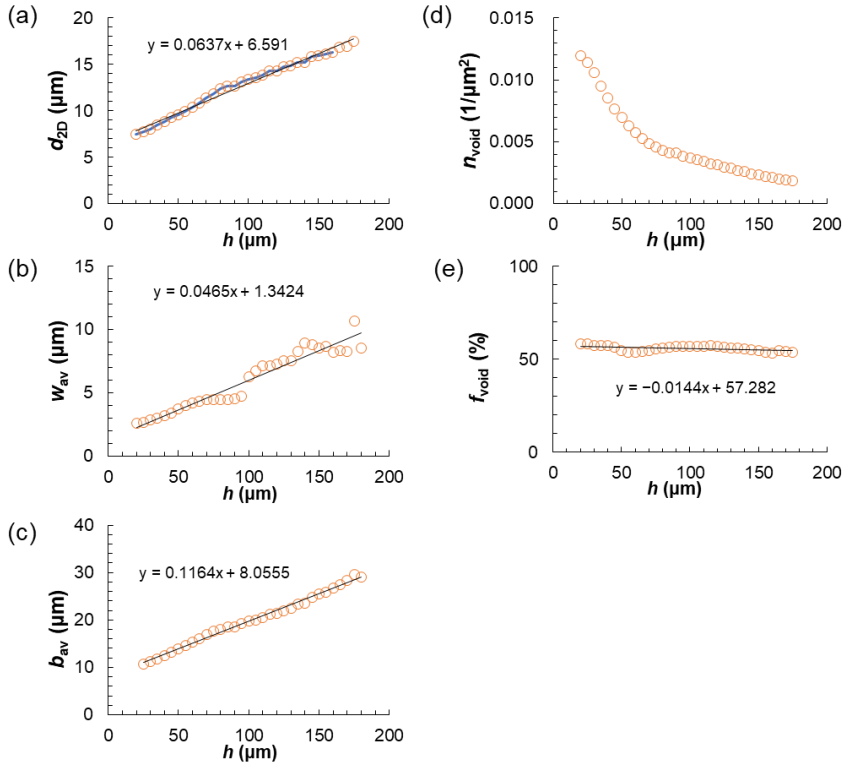

Figure 3. Depth profiles of macrovoid characteristics calculated from each two-dimensional development view as functions of depth, h, from the surface. (a) Average macrovoid equivalent circular diameter, d_{2D}. (b) Mean local thickness of the polymer skeleton, w_{av}. (c) Average distance between neighboring macrovoids, b_{av}. (d) Macrovoid number density, n_{void}. (e) Macrovoid percentage, f_{void}.

3.3.Comparison Between Surface and Internal Macrovoids

Previous studies on NIPS membranes have shown that increasing the polymer concentration in the dope solution[6–8] and/or adding coagulant water to the doped polymer solution[10–12] promotes the formation of a thick skin layer. Accordingly, we prepared two types of PAN fiber: PAN-20, spun from a solution with a high (20 wt%) polymer concentration, and PAN-15w, spun from a dope solution containing 15 wt% PAN and 5.0% water in DMSO. Their SEM images were shown in Figure S2. The CT tomograms of PAN-20 and PAN-15w show thick skin layers with L_{skin} values of 46.9 and 37.7 μm, respectively (Figure 4a); these skin layers are much thicker than that of PAN-15, consistent with the results of previous SEM-based studies [8,11]. The ϕ_{bulk} values of PAN-20 and PAN-15w were determined to be 68.5 and 76.2%, respectively, which are almost the same as that of PAN-15.

Although they shared the common characteristic of a thick L_{skin} and similar ϕ_{bulk} values (Table 1), PAN-20 and PAN-15w have significantly different macrovoid morphologies when imaged using micro-CT (Figure 4a, b). PAN-20 has a heterogeneous morphology consisting of large and small macrovoids, whereas PAN-15w contains uniformly distributed macrovoids that are almost identical in size. Differences are quantitatively presented in the d_{2D} distributions (Figure 4c); PAN-20 exhibits a broad bimodal d_{2D} distribution, whereas PAN-15w shows a single narrow distribution. These results suggest that while macroscopic structural parameters such as ϕ_{bulk} and L_{skin} are useful, they do not fully capture the differences in the macrovoid structural characteristics, and that local structural information obtained using micro-CT provides valuable information. The ϕ_{CT} values of PAN-20 and PAN-15w were determined to be 23.2 and 32.1%, respectively, which are somewhat smaller than that of PAN-15 (44.6%). The lower ϕ_{CT} values observed for the former are consistent with a larger polymer-skeleton volume; however, the corresponding ϕ_{bulk} values are similar, resulting from the higher $\phi_{skeleton}$ (Table 1).

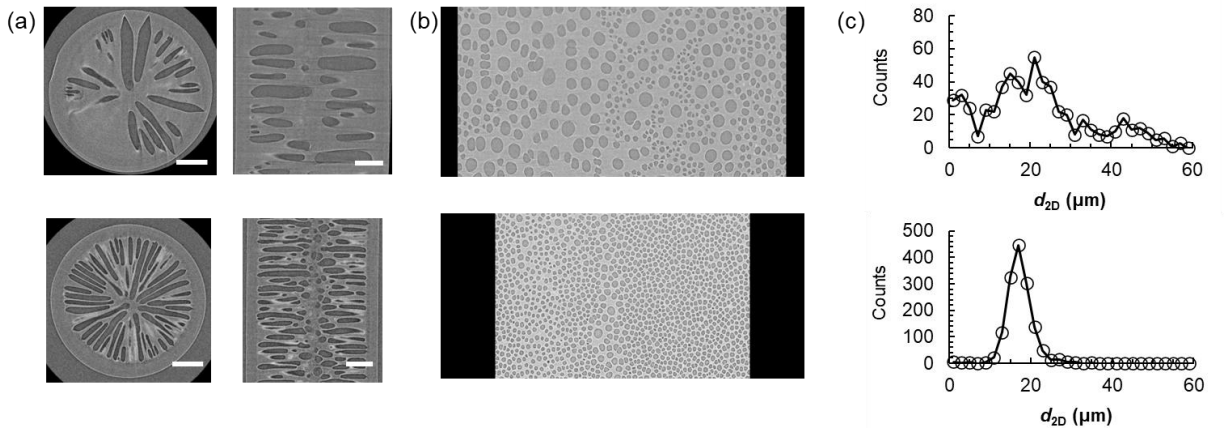

Figure 4. Macrovoid morphologies of PAN fibers determined by micro-CT: PAN-20 (upper) and PAN-15w (lower). (a) Tomograms orthogonal to (left) and along (right) the fiber axis. Scale bars are 100 μm. (b) Development views at h = 100 μm. (c) Equivalent circular diameter, d_{2D}, distributions of the macrovoids of the panel (c).

Volume-rendered images of macrovoids projected along the fiber axis were generated by rendering the PAN skeleton highly transparent and overlaying the surface skin layer in semi-transparent gray (Figure 5a,b). In the PAN-20 fiber, large macrovoids shown in blue were found to initiate near the surface and grow inward by penetrating the skin layer, whereas smaller macrovoids shown in green predominantly initiated beneath the skin layer (Figure 5a). These images clearly demonstrate the coexistence of two distinct types of macrovoids: those initiating near the surface and those forming beneath the skin layer. Hereafter, we refer to these as "surface macrovoids" and "internal (sub-skin) macrovoids", respectively. The initiation points of surface macrovoids are not captured in the example tomograms shown in Figure 4a. This is because these initiation points exist as localized single points in three-dimensional space, making the probability that an arbitrary cross section intersects such a point extremely low. Consequently, when macrovoids are examined using cross-sectional images, surface macrovoids are nearly indistinguishable from internal macrovoids. In contrast, the volume-rendered images projected

along the fiber axis clearly reveal the initiation positions of macrovoids near the surface, highlighting the importance of appropriate three-dimensional visualization for accurate macrovoid classification.

Figure 5b shows that, in the PAN-15w fiber, most macrovoids, shown in both blue and green, grow from beneath the skin layer in a dense and spatially uniform manner, regardless of size, indicating that they are predominantly internal macrovoids. Only a few surface macrovoids shown in blue initially expand as they penetrate the skin layer owing to their low number density; however, beneath the skin layer, their growth is restricted by competition with internal macrovoids, resulting in nearly constant diameters.

Surface and internal macrovoids differ not only in their initiation positions but also in their morphologies near the initiation points (Figure 5c). Surface macrovoids exhibit sharp initiation tips, whereas internal macrovoids display rounded initiation geometries, suggesting that distinct formation mechanisms are responsible for generating the two macrovoid types. Specifically, the difference in tip shape originates from the initiation density of macrovoids: tips become sharper at low initiation densities and smoother at high initiation densities. The internal macrovoids shown in green in the PAN-20 fiber are generally shorter than the surface macrovoids (Figure 5a), indicating that their growth is terminated by competitive growth with the large surface macrovoids shown in blue.

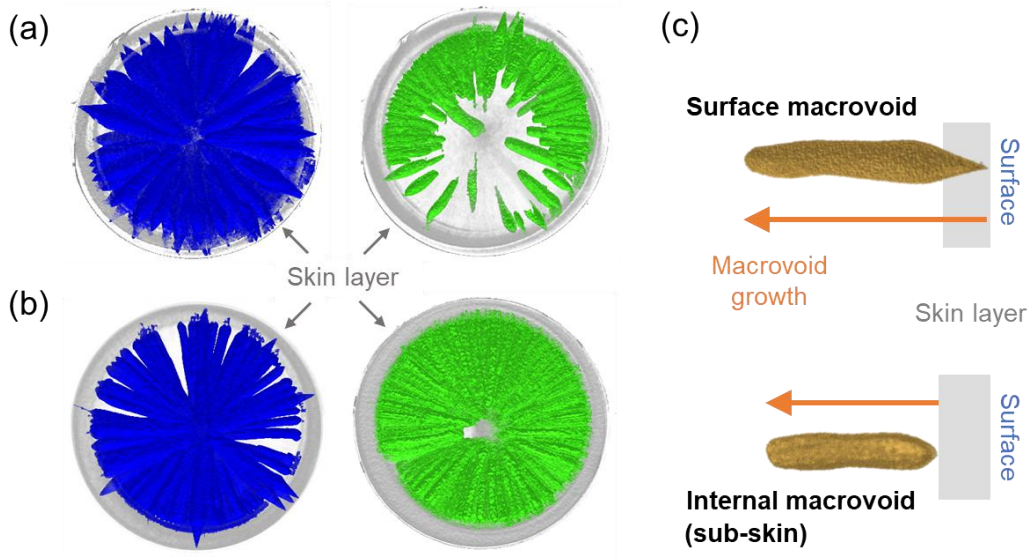

Figure 5. (a, b) Volume-rendered images of macrovoids projected along the fiber axis: (a) PAN-20 and (b) PAN-15w. The blue and green macrovoids have d_{3D} >50 μm and 20 ≤ d_{3D} ≤ 50 μm, respectively. These macrovoids were drawn by rendering the PAN skeleton highly transparent and overlaying the surface skin layer in semi-transparent gray. (c) Representative macrovoids in PAN-20: a surface macrovoid initiated on the surface of the fiber (upper) and an inner macrovoid initiated from beneath the skin layer (lower).

3.4. Depth Profiles of Macrovoid Structural Parameters for Thick-Skinned Fibers

Micro-CT analysis further enables quantitative evaluation of the depth-dependent structural parameters of macrovoids (Figure 6). In PAN-20, surface macrovoids are present within the thick skin layer up to h = 47 μm; however, f_{void} remains very small owing to the low n_{void} and d_{2D} values. Beyond the skin layer, f_{void} gradually increases with increasing h as internal macrovoids form, and then reaches a steady state at h ≈ 80 μm. With increasing h, d_{2D} increases, whereas n_{void} decreases. In PAN-15w, macrovoids first appear at h = 38 μm, corresponding to the end of the skin layer. Beyond the skin layer, n_{void} decreases while f_{void} increases sharply up to h = 60 μm. At greater h, f_{void}, d_2, n_{void}, and w_{av} reach nearly constant values.

Comparison of PAN-15w and PAN-20 with PAN-15 at h = 80 μm, where these parameters plateau, reveals that PAN-15w exhibits an f_{void} value comparable to that of PAN-15 (53% for PAN-15w and 57% for PAN-15). In contrast, PAN-20 shows a significantly lower f_{void} of 39%, accompanied by a low n_{void}, large d_{2D}, and thick w_{av}. These results demonstrate that three-dimensional micro-CT data enables clear discrimination between surface and internal macrovoids by revealing their distinct depth-dependent structural characteristics, which cannot be resolved using conventional two-dimensional analyses.

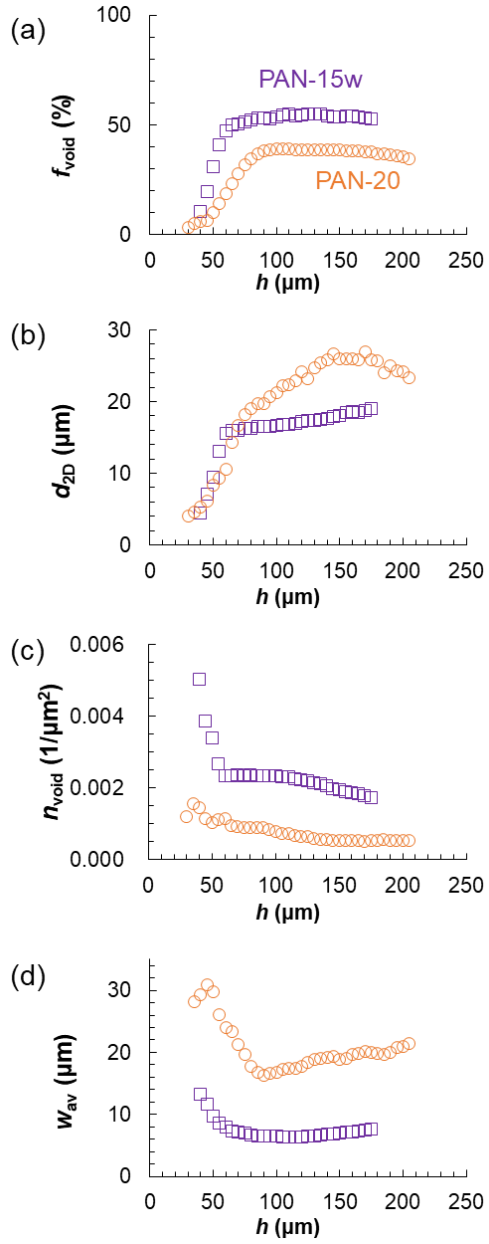

Figure 6. Depth profiles of macrovoid structural characteristics calculated from each two-dimensional development view as functions of depth h from the surface: PAN-20 (orange circles) and PAN-15w (purple squares). (a) Macrovoid percentage, f_{void}. (b) Average macrovoid equivalent circular diameter, d_{2D}. (c) Macrovoid number density, n_{void}. (d) Mean local thickness of the polymer skeleton, w_{av}.

3.5.Schematic Illustrations of Macrovoids for Thin and Thick-skinned Fibers

The macrovoid structures observed in this study are schematically summarized in Figure 7. In PAN-15, most macrovoids initiate almost simultaneously beneath the thin skin layer, very close to the surface, and grow along the depth direction, leading to strong competitive growth between adjacent macrovoids (Figure 7a). As a result, only a limited number of macrovoids continue to grow inwards, whereas the growth of neighboring macrovoids is suppressed. This competitive growth process leads to larger in-plane cross-sections and a progressive decrease in macrovoid number density with increasing depth from the surface (Figure 3).

This interpretation is partially consistent with the schematic proposed by Matz et al.[19], in which macrovoids grow densely and in parallel. Similar concepts of simultaneous initiation and competitive growth during phase inversion have been discussed in the early stage of experimental studies of finger-like structure formation [20,25]. The simulation by Deng et al.[30] reproduced the initial stage of surface macrovoid formation. However, these previous schematics did not explicitly capture the selective survival of macrovoids, where small macrovoids remain confined to shallow regions owing to growth inhibition caused by competition.

In PAN-20, a thick skin layer is formed near the surface (Figure 7b). Only a small number of surface macrovoids are sparsely initiated at the surface, penetrate the skin layer, and grow along the depth direction while expanding laterally. This expansion at the tip of surface macrovoids is consistent with the schematic diagram proposed by Guillen et al. [5]. Beneath the thick skin layer, internal macrovoids initiate simultaneously between the surface macrovoids. These internal macrovoids grow competitively with the surface macrovoids, which restricts their lateral expansion beneath the skin layer. Surface macrovoids exhibit sharp initiation tips, whereas internal macrovoids display rounded initiation geometries. Internal macrovoids have previously been schematically illustrated by Smolders et al.[10] and Koros et al.[24]. While these studies

captured key features of internal macrovoids, they did not include coexistence with surface and internal macrovoids, nor their competitive growth and quantitative analysis.

PAN-15w also possesses a macrovoid-free, thick skin layer; therefore, most of its macrovoids are internal ones that initiate beneath the thick skin layer (Figure 7c). These internal macrovoids nucleate densely and grow nearly simultaneously along the depth direction, resulting in straight macrovoids with uniform diameters and high porosities. The internal macrovoids observed in PAN-15w are structurally similar to those formed in PAN-20, suggesting a common underlying formation mechanism governed by internal phase separation and subsequent competitive growth as proposed previously [10,24].

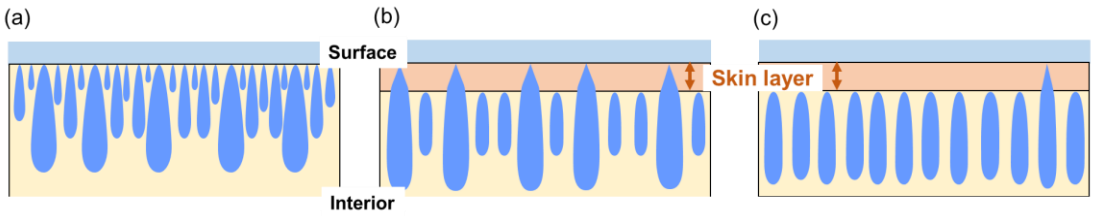

Figure 7. Schematic illustration of surface and internal macrovoids supported by 3D experimental evidence. The macrovoids formed under different fabrication conditions: (a) PAN-15, (b) PAN-20, and (c) PAN-15w.

Across the three fibers fabricated under different conditions in this study, almost all macrovoids are formed either below the thin skin layer at the surface or directly beneath the thick skin layer. These observations indicate that macrovoid formation is not spatially random but occurs deterministically under thermodynamic conditions and kinetic pathways [2]. In the present study, we focused on a single solvent–nonsolvent pair (DMSO/water). Solvent effects are currently under investigation and will be reported separately.

The presence or absence of fractured-driven fine channels within the skin layers, as proposed by Strassmann et al.[7], could not be confirmed due to the limited spatial resolution of micro-CT. In general, three-dimensional real-space imaging techniques involve a trade-off between field of view and spatial resolution for hierarchical nano- and macroporous structures.[45] X-ray micro-CT provides a sufficiently large field of view to visualize macrovoid architectures in three dimensions, but its resolution is insufficient to directly resolve nanoscale porosity within the polymer skeleton. Therefore, micro-CT is most effective when complemented by higher-resolution techniques such as SEM [42] or PXCT [36] for hierarchical nano- and macroporous structures. Numerous schematic illustrations describing macrovoid formation have been proposed in the literature [5,7,10,19,24,25]; however, none capture all of the structural characteristics revealed in this study using micro-CT.[36] By directly visualizing macrovoids in three dimensions with a sufficiently large field of view and adequate spatial resolution, the present micro-CT analysis allows us to propose comprehensive, experimentally supported schematics of macrovoid architectures.

4. CONCLUSIONS

In this study, macrovoid structures in polyacrylonitrile fibers wet-spun by NIPS were visualized and quantitatively analyzed using high-resolution X-ray micro-CT. Three-dimensional imaging over a wide field of view revealed that macrovoids are not randomly distributed throughout the fiber but preferentially initiate either at the fiber surface or beneath the thick skin layer, depending on fabrication conditions. Two distinct types of macrovoids were identified. Surface macrovoids initiate at or near the surface and exhibit sharp initiation tips, whereas internal macrovoids nucleate beneath the thick skin layer and display rounded initiation geometries. Quantitative depth-resolved analysis demonstrated that the number density, size

evolution, and spatial distributions of these macrovoid types are governed by polymer concentration and dope-solution composition. In particular, competitive growth between surface and internal macrovoids beneath the skin layer plays a critical role in determining macrovoid morphology, number density, and depth-dependent structural parameters. The results demonstrate that three-dimensional micro-CT analysis enables accurate identification and classification of macrovoid types, which cannot be achieved using conventional two-dimensional techniques. The mechanistic insights obtained in this study provide a structural basis for rational control and optimization of macrovoid architectures, contributing to the development of advanced asymmetric membranes and hollow fibers fabricated via NIPS and wet-spinning processes.

ASSOCIATED CONTENT

Supporting Information

The Supporting Information is available free of charge.

Volume-rendered and fiber-axis–projected macrovoid images in PAN-15 with macrovoid size classes (Figure S1); Cross-sectional SEM micrographs of PAN fibers (full cross-sections, near-surface region, and PAN skeleton between adjacent macrovoids) (Figure S2); Full description of experimental section; Fabrication conditions for PAN-15, PAN-20, and PAN-15w fibers prepared by NIPS (Table S1) (PDF).

Author Contributions

Sadaki Samitsu: Conceptualization, Methodology, Writing - Original Draft, Writing - Review & Editing, Visualization, Supervision, Project administration, Funding acquisition. **Misa Hazutani:** Investigation, Data Curation. **Miwa Ohniwa:** Investigation.

Funding

This work was supported by the Japan Science and Technology Agency (JST), CREST, Grant Number JPMJCR23L2 (S.S.), "Precise Material Science for Degradation and Stability", and by the Ministry of Education, Culture, Sports, Science and Technology (MEXT), Grant Number JPMXP1122714694 (S.S.), Data Creation and Utilization-Type Material Research and Development Project.

ACKNOWLEDGMENTS

The authors thank Prof. Dr. Masanobu Naito of NIMS for instrumental support with X-ray micro-CT. The authors would like to express sincere gratitude to Mr. Masaru Anahara of Kaneka Corporation for valuable discussions regarding the phase separation behavior of polymer solutions.

REFERENCES

(1) van de Witte, P.; Dijkstra, P. J.; van den Berg, J. W. A.; Feijen, J. Phase separation processes in polymer solutions in relation to membrane formation. **J. Membr. Sci.** *1996*, **117**, 1–31.

(2) Guillen, G. R.; Pan, Y.; Li, M.; Hoek, E. M. V. Preparation and characterization of membranes formed by nonsolvent induced phase separation: A review. **Ind. Eng. Chem. Res.** *2011*, **50**, 3798–3817.

(3) Hołda, A. K.; Vankelecom, I. F. J. Understanding and guiding the phase inversion process for synthesis of solvent resistant nanofiltration membranes. **J. Appl. Polym. Sci.** *2015*, **132**, 42130.

(4) Shirvan, A. R.; Nouri, A.; Sutti, A. A perspective on the wet spinning process and its advancements in biomedical sciences. **Eur. Polym. J.** *2022*, **181**, 111681.

(5) Guillen, G. R.; Ramon, G. Z.; Kavehpour, H. P.; Kaner, R. B.; Hoek, E. M. V. Direct microscopic observation of membrane formation by nonsolvent induced phase separation. **J. Membr. Sci.** *2013*, **431**, 212–220.

(6) Matz, R. The structure of cellulose acetate membranes 1. The development of porous structures in anisotropic membranes. **Desalination** *1972*, **10**, 1–15.

(7) Strathmann, H.; Kock, K.; Amar, P.; Baker, R. W. The formation mechanism of asymmetric membranes. **Desalination** *1975*, **16**, 179–203.

(8) Pekny, M. R.; Zartman, J.; Krantz, W. B.; Greenberg, A. R.; Todd, P. Flow-visualization during macrovoid pore formation in dry-cast cellulose acetate membranes. **J. Membr. Sci.** *2003*, **211**, 71–90.

(9) Maggay, I. V.; Yu, M.-L.; Wang, D.-M.; Chiang, C.-H.; Chang, Y.; Venault, A. Strategy to prepare skin-free and macrovoid-free polysulfone membranes via the NIPS process. **J. Membr. Sci.** *2022*, **655**, 120597.

(10) Hung, W.-L.; Wang, D.-M.; Lai, J.-Y.; Chou, S.-C. On the initiation of macrovoids in polymeric membranes: Effect of polymer chain entanglement. **J. Membr. Sci.** *2016*, **505**, 70–81.

(11) Frommer, M. A.; Messalem, R. M. Mechanism of membrane formation. VI. Convective flows and large void formation during membrane precipitation. **Ind. Eng. Chem. Prod. Res. Dev.** *1973*, **12**, 328–333.

(12) Matveev, D.; Vasilevsky, V.; Volkov, V.; Plisko, T.; Shustikov, A.; Volkov, A.; Bildyukevich, A. Fabrication of ultrafiltration membranes from non-toxic solvent

dimethylsulfoxide: Benchmarking of commercially available acrylonitrile co-polymers. **J. Environ. Chem. Eng.** *2022*, **10**, 107061.

(13) Smolders, C. A.; Reuvers, A. J.; Boom, R. M.; Wienk, I. M. Microstructures in phase-inversion membranes. Part 1. Formation of macrovoids. **J. Membr. Sci.** *1992*, **73**, 259–275.

(14) Kahrs, C.; Gühlstorf, T.; Schwellenbach, J. Influences of different preparation variables on polymeric membrane formation via nonsolvent induced phase separation. **J. Appl. Polym. Sci.** *2020*, **137**, 48852.

(15) Yanagishita, H.; Nakane, T.; Yoshitome, H. Selection criteria for solvent and gelation medium in the phase inversion process. **J. Membr. Sci.** *1994*, **89**, 215–221.

(16) Kang, Y. S.; Kim, H. J.; Kim, U. Y. Asymmetric membrane formation via immersion precipitation method. I. Kinetic effect. **J. Membr. Sci.** *1991*, **60**, 210–232.

(17) Samitsu, S.; Pruksawan, S.; Yokoyama, H.; Ichinose, I. Solvent effects during the flash-freezing fabrication of mesoporous polystyrenes. **Macromolecules** *2022*, **55**, 3734–3746.

(18) Boom, R. M.; Wienk, I. M.; van den Boomgaard, T.; Smolders, C. A. Microstructures in phase inversion membranes. Part 2. The role of a polymeric additive. **J. Membr. Sci.** *1992*, **73**, 277–292.

(19) Sadrzadeh, M.; Bhattacharjee, S. Rational design of phase inversion membranes by tailoring thermodynamics and kinetics of casting solution using polymer additives. **J. Membr. Sci.** *2013*, **441**, 31–44.

(20) Paulsen, F. G.; Shojaie, S. S.; Krantz, W. B. Effect of evaporation step on macrovoid formation in wet-cast polymeric membranes. **J. Membr. Sci.** *1994*, **91**, 265–282.

(21) Ray, R. J.; Krantz, W. B.; Sani, R. L. Linear stability theory model for finger formation in asymmetric membranes. **J. Membr. Sci.** *1985*, **23**, 155–182.

(22) Termonia, Y. Fundamentals of polymer coagulation. **J. Polym. Sci., Part B: Polym. Phys.** *1995*, **33**, 279–288.

(23) Ren, J.; Li, Z.; Wong, F.-S. Membrane structure control of BTDA-TDI/MDI (P84) co-polyimide asymmetric membranes by wet-phase inversion process. **J. Membr. Sci.** *2004*, **241**, 305–314.

(24) Hopp-Hirschler, M.; Safdari Shadloo, M.; Nieken, U. Viscous fingering phenomena in the early stage of polymer membrane formation. **J. Fluid Mech.** *2019*, **864**, 97–140.

(25) McKelvey, S. A.; Koros, W. J. Phase separation, vitrification, and the manifestation of macrovoids in polymeric asymmetric membranes. **J. Membr. Sci.** *1996*, **112**, 29–39.

(26) Garcia, J. U.; Iwama, T.; Chan, E. Y.; Tree, D. R.; Delaney, K. T.; Fredrickson, G. H. Mechanisms of asymmetric membrane formation in nonsolvent-induced phase separation. **ACS Macro Lett.** *2020*, **9**, 1617–1624.

(27) Cervellere, M. R.; Qian, X.; Ford, D. M.; Carbrello, C.; Giglia, S.; Millett, P. C. Phase-field modeling of nonsolvent induced phase separation (NIPS) for PES/NMP/water with comparison to experiments. **J. Membr. Sci.** *2021*, **619**, 118779.

(28) Ahmad, T.; Rehman, L. M.; Al-Nuaimi, R.; de Levay, J. P. B. B.; Thankamony, R.; Mubashir, M.; Lai, Z. Thermodynamics and kinetic analysis of membrane: Challenges and perspectives. **Chemosphere** *2023*, **337**, 139430.

(29) Lin, H.-H.; Tang, Y.-H.; Matsuyama, H.; Wang, X.-L. Dissipative particle dynamics simulation on the membrane formation of polymer–solvent system via nonsolvent induced phase separation. **J. Membr. Sci.** *2018*, **548**, 288–297.

(30) Deng, X.; Zhao, Y.; Yang, F.; Li, Y.; Ouyang, M. Hydrodynamics coupled simulation of fingerlike pore formation during nonsolvent induced phase separation. **Langmuir** *2025*, **41**, 13107–13118.

(31) Hopp-Hirschler, M.; Nieken, U. Modeling of pore formation in phase inversion processes: Model and numerical results. **J. Membr. Sci.** *2018*, **564**, 820–831.

(32) Tree, D. R.; Iwama, T.; Delaney, K. T.; Lee, J.; Fredrickson, G. H. Marangoni flows during nonsolvent induced phase separation. **ACS Macro Lett.** *2018*, **7**, 582–586.

(33) Chen, V.; Li, H.; Fane, A. G. Non-invasive observation of synthetic membrane processes: A review of methods. **J. Membr. Sci.** *2004*, **241**, 23–44.

(34) Manickam, S. S.; Gelb, J.; McCutcheon, J. R. Pore structure characterization of asymmetric membranes: Non-destructive characterization of porosity and tortuosity. **J. Membr. Sci.** *2014*, **454**, 549–554.

(35) Remigy, J. C.; Meireles, M.; Thibault, X. Morphological characterization of a polymeric microfiltration membrane by synchrotron radiation computed microtomography. **J. Membr. Sci.** *2007*, **305**, 27–35.

(36) Górecki, R.; Polo, C. C.; Kalile, T. A.; Miqueles, E. X. S.; Tonin, Y. R.; Upadhyaya, L.; Meneau, F.; Nunes, S. P. Ptychographic X-ray computed tomography of porous membranes with nanoscale resolution. **Commun. Mater.** *2023*, **4**, 68.

(37) Rudolph-Schöpping, G.; Larsson, E.; Pingel, T. N.; Guizar-Sicairos, M.; Villanueva-Perez, P.; Hall, S.; Lipnizki, F. Towards multiscale X-ray tomographic imaging in membrane science—A perspective. **J. Membr. Sci.** *2024*, **690**, 122245.

(38) Li, D.; Zhai, J.; Wang, K.; Shen, Y.; Huang, X. Three-dimensional reconstruction-characterization of polymeric membranes: A review. **Environ. Sci. Technol.** *2025*, **59**, 2891–2916.

(39) Brickey, K. P.; Zydney, A. L.; Gomez, E. D. FIB-SEM tomography reveals the nanoscale 3D morphology of virus removal filters. **J. Membr. Sci.** *2021*, **640**, 119766.

(40) Samitsu, S.; Zhang, R.; Peng, X.; Krishnan, M. R.; Fujii, Y.; Ichinose, I. Flash freezing route to mesoporous polymer nanofibre networks. **Nat. Commun.** *2013*, **4**, 2653.

(41) George, A.; Hazutani, M.; Samitsu, S.; Gowd, E. B. Tuning Crystal Structure, Orientation, and Morphology in Nylon-11 Aerogels via Freezing Rate Modulation during Unidirectional Freezing. **ACS Appl. Polym. Mater.** *2026*, **8**, 3144–3157.

(42) Ono, T.; Samitsu, S.; Hazutani, M.; Ata, S. Structural characterization of hierarchical polymer foams by combining X-ray micro-computed tomography and scanning electron microscopy. **Polym. Test.** *2024*, **140**, 108580.

(43) Ding, S. G.; Cheng, X. Q.; Jiang, Z. X.; Bai, Y. P.; Shao, L. Pore morphology control and hydrophilicity of polyacrylonitrile ultrafiltration membranes. **J. Appl. Polym. Sci.** *2015*, **132**, 41991.

(44) Nebesskaya, A.; Kanateva, A.; Borisov, R.; Yushkin, A.; Volkov, V.; Volkov, A. Polyacrylonitrile ultrafiltration membrane for separation of used engine oil. **Polymers** *2024*, **16**, 2910.

(45) Burnett, T. L.; Kelley, R.; Winiarski, B.; Contreras, L.; Daly, M.; Gholinia, A.; Burke, M. G.; Withers, P. J. Large Volume Serial Section Tomography by Xe Plasma FIB Dual Beam Microscopy. **Ultramicroscopy** *2016*, **161**, 119–129.